

Cite this article as:

Touska P, Connor SEJ. Recent advances in MRI of the head and neck, skull base and cranial nerves: new and evolving sequences, analyses and clinical applications. *Br J Radiol* 2019; **92**: 20190513.

## REVIEW ARTICLE

# Recent advances in MRI of the head and neck, skull base and cranial nerves: new and evolving sequences, analyses and clinical applications

<sup>1</sup>PHILIP TOUSKA, FRCR and <sup>1,2,3</sup>STEVE E. J. CONNOR, FRCR

<sup>1</sup>Department of Radiology, Guy's and St. Thomas' NHS Foundation Trust, Guy's Hospital, Great Maze Pond, London, SE1 9RT, United Kingdom

<sup>2</sup>Department of Neuroradiology, Kings College Hospital NHS Trust, Denmark Hill London SE5 9RS, United Kingdom

<sup>3</sup>School of Biomedical Engineering & Imaging Sciences Clinical Academic Group, King's College London, UK

Address correspondence to: Dr Philip Touska

E-mail: [p.touska@nhs.net](mailto:p.touska@nhs.net)

### ABSTRACT:

MRI is an invaluable diagnostic tool in the investigation and management of patients with pathology of the head and neck. However, numerous technical challenges exist, owing to a combination of fine anatomical detail, complex geometry (that is subject to frequent motion) and susceptibility effects from both endogenous structures and exogenous implants. Over recent years, there have been rapid developments in several aspects of head and neck imaging including higher resolution, isotropic 3D sequences, diffusion-weighted and diffusion-tensor imaging as well as permeability and perfusion imaging. These have led to improvements in anatomic, dynamic and functional imaging. Further developments using contrast-enhanced 3D FLAIR for the delineation of endolymphatic structures and black bone imaging for osseous structures are opening new diagnostic avenues. Furthermore, technical advances in compressed sensing and metal artefact reduction have the capacity to improve imaging speed and quality, respectively. This review explores novel and evolving MRI sequences that can be employed to evaluate diseases of the head and neck, including the skull base.

### INTRODUCTION

The structures of the head and neck, including the skull base, pose a multitude of technical challenges with respect to the application of MRI techniques. In particular, multiple complex anatomical structures exist in a small volume, which demands high resolution; however, speed is also essential owing to the intrinsic mobility of cervical tissues involved in respiration and deglutition. Furthermore, natural air-filled cavities, bone-soft tissue interfaces and the presence of exogenous metallic implants or dental restorations result in magnetic susceptibility effects that can degrade image quality. In addition, standard anatomical sequences can be limited in their ability to reliably differentiate benign from malignant tissues (*e.g.*, in assessing tumour response to chemoradiotherapy (CTR)), delineating neural structures (*e.g.*, cranial nerves displaced by tumours or surrounded by pneumatized bone) and the differentiation of anatomical compartments (*e.g.*, endolymphatic and perilymphatic labyrinthine fluid). As a result, over the last decade, significant strides have been made towards addressing the aforementioned challenges.

The following review discusses new and evolving MRI sequences, and how they are applied to head and neck, cranial nerve and skull base imaging scenarios.

### HIGH-RESOLUTION 3D T2-WEIGHTED SEQUENCES

Highly fluid-sensitive (sometimes termed cisternographic) sequences offer high spatial and contrast resolution and can be used to depict the cisternal portions of cranial nerves as well as the structures of the fluid-filled labyrinth. They are based upon either fast gradient echo or fast spin-echo (FSE) techniques, and some of the commonly encountered sequences are included in [Table 1](#).

Fast gradient echo sequences are typically susceptible to dephasing related to small field inhomogeneities, resulting in linear low-signal (banding) artefacts, which may simulate lesions within the internal auditory canal and labyrinth, although this effect is reduced by performing two acquisitions with and without phase frequency alternations in the Constructive interference into steady state and fast

Table 1. Types of 3D T<sub>2</sub>-weighted sequences

Fast Gradient Echo	Fast Spin Echo
3D fully refocussed (balanced) steady-state free precession: <ul style="list-style-type: none"> <li>• TrueFISP (fast imaging with steady-state precession) - Siemens</li> <li>• Fast imaging employing steady-state acquisition (FIESTA) - GE</li> <li>• Balanced FFE (fast field echo) - Philips</li> </ul>	Rapid recovery of longitudinal magnetisation through a 90 degree RF pulse at the end of the echo train (driven equilibrium): <ul style="list-style-type: none"> <li>• RESTORE - Siemens</li> <li>• FRFSE (fast recovery fast spin echo) - GE</li> <li>• DRIVE - Philips</li> </ul>
MIP of two consecutive TrueFISP (fast imaging in steady state precession) sequences of alternating and non-alternating RF pulses: <ul style="list-style-type: none"> <li>• CISS (Constructive interference into steady state) - Siemens</li> <li>• Fast imaging employing steady-state acquisition with phase cycling (FIESTA-C) - GE</li> </ul>	Special 3D FSE technique <ul style="list-style-type: none"> <li>• Sampling perfection with application-optimized contrasts by using different flip angle evolutions) - Siemens</li> <li>• CUBE - GE</li> <li>• Volume ISotropic Turbo spin echo Acquisition (VISTA) - Philips</li> </ul>

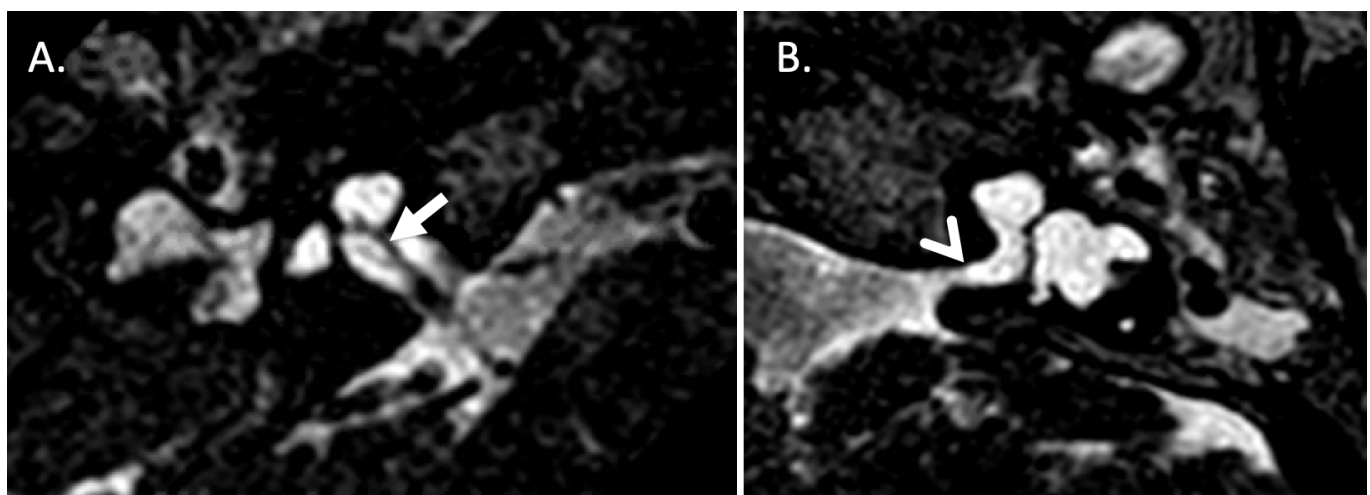
imaging employing steady-state acquisition with phase cycling sequences.<sup>1</sup>

By virtue of multiple 180 degree refocussing pulses, FSE techniques are insensitive to susceptibility artefacts, but typically involve longer scanning times and can be susceptible to blurring. As an alternative, special FSE techniques such as SPACE, VISTA or CUBE (Table 1) can be employed. These are characterised by short, non-spatially selective radiofrequency pulses (significantly shortening the echo spacing) and variable flip angles for refocusing radiofrequency pulses (suppressing blurring whilst reducing flow and chemical shift artefacts). They are capable of isotropic imaging up to 0.3 mm at 3T and provide higher CNR when compared with TrueFISP.<sup>2,3</sup>

The clinical applications of high-resolution 3D T<sub>2</sub>W imaging are wide-ranging and have become routine in otologic imaging where they are capable of demonstrating labyrinthine anomalies with increased sensitivity<sup>4</sup> and obviate the requirement for CT in the setting of childhood sensorineural hearing loss (SNHL) (Figure 1).<sup>5</sup> They are also useful in the pre-operative assessment of cochlear implant candidates, confirming patency of the

cochlear aperture, delineating cochlear nerve calibre and determining cochlear size for electrode length and positioning.<sup>6-8</sup> Furthermore, such sequences are effective both as screening and follow-up tools in the case of vestibular schwannomas. In the latter setting, there is increasing evidence that non-contrast 3D T<sub>2</sub>W sequences can provide a cost-effective alternative to gadolinium-enhanced T<sub>1</sub>W sequence for the detection and monitoring of vestibular schwannomas.<sup>9,10</sup> Non-contrast MRI cisternography can also provide a non-invasive approach to the diagnosis of CSF leaks in the context of suspected CSF rhinorrhoea or otorrhea with a sensitivity in excess of 76%.<sup>11</sup> In such cases, CSF isointense signal can be seen to traverse the skull base. Similarly, post-traumatic labyrinthine fistulae may be detected using MR cisternography, which may be missed on CT studies.<sup>12</sup> 3D high-resolution iT<sub>2</sub>W imaging is also considered the reference standard for imaging in neurovascular conflict, enabling confirmation of contact in the transition zone (between central and peripheral myelin), which is vulnerable to compression.<sup>13</sup> This has roles in identifying vascular compression in trigeminal neuralgia and other neurovascular syndromes including hemifacial spasm and vestibular paroxysmia, where the location of contact and degree of deformity can be identified.<sup>14-16</sup>

Figure 1. 3D T<sub>2</sub>-weighted DRIVE sequence with a resolution of 0.3 mm through the internal auditory meati (IAM) with bilateral sensorineural hearing loss and right-sided microtia being considered for cochlear implantation. A. Oblique axial sequence confirms the presence of a cochlear nerve within the right IAM (solid arrow). B. Oblique axial sequence at the same level demonstrates no visible nerve is seen within the left IAM. Features of incomplete partition Type one are seen bilaterally with a hypoplastic modiolus on the right and absent modiolus on the left (open arrow).



Finally, 3D high-resolution T2W sequences have been employed at ultrahigh (7T) field strengths to delineate labyrinthine and internal auditory canal anatomy and exclude compressive structural lesions in neurovascular conflict syndromes, such as vestibular paroxysmia.<sup>17,18</sup> However, several technical challenges remain, including increased susceptibility artefacts and specific absorption rate limitations.<sup>19</sup>

### FAT SUPPRESSION

The anatomical complexity and relative abundance of fat within the cervical soft tissues make fat suppression techniques invaluable for the evaluation of head and neck pathology, particularly in the detection of perineural tumoural spread.<sup>20</sup> A wide variety of techniques are available, including short-tau inversion recovery (STIR), 3-point Dixon and, more recently, 3D techniques. These have largely replaced traditional selective (spectral) fat suppression techniques, which are highly sensitive to field inhomogeneities.<sup>21,22</sup> Less frequently, selective excitation of water protons can be used to reduce signal from fat protons and obviate the need for fat saturation. There has been limited use of this technique in the head and neck, but a double-echo steady-state sequence with water excitation has demonstrated some promise in delineating the intraparotid facial nerve.<sup>23</sup>

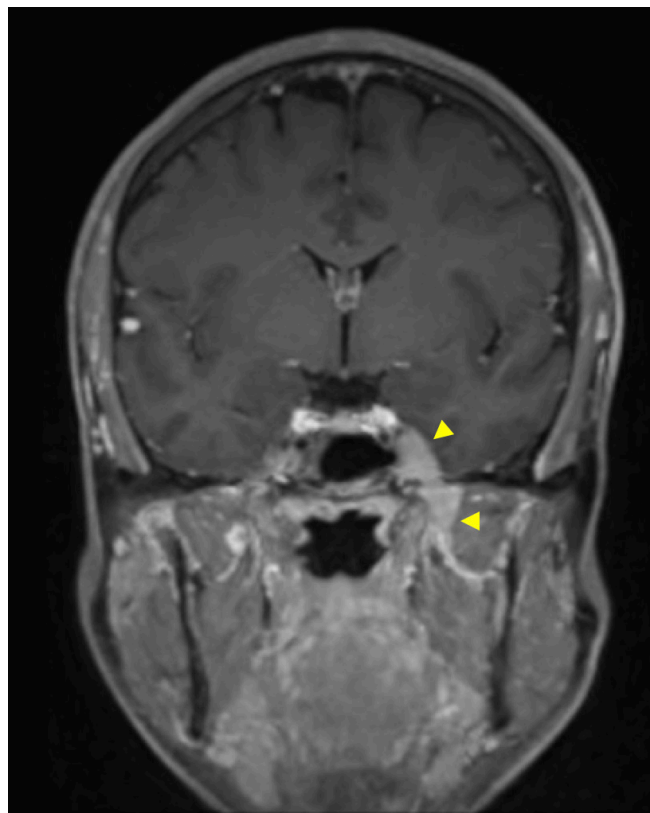
### 3D ISOTROPIC GADOLINIUM-ENHANCED SEQUENCES

Sequences acquiring contiguous isotropic (3D) data offer benefits in head and neck imaging as a single acquisition can provide data for reformatting in any plane, obviating the need for multiple separate sequences.<sup>24</sup> The mainstay of 3D sequences are ultra-fast spoiled GE sequences with small flip angles and short TR. These typically have pre-pulses (magnetisation preparation) to provide T1W and T2W or fat suppression and can be combined with partial k-space sampling to further reduce acquisition times; examples include volumetric interpolated breath-hold examination (VIBE) from Siemens and T1W high-resolution isotropic volume examination from Philips.<sup>25</sup> These are capable of achieving more accurate pre-operative estimation of head and neck tumour size compared with 2D acquisitions, but susceptibility artefacts are problematic.<sup>25</sup> Sensitivity to bulk motion can be reduced by applying overlapping radial (as opposed to standard cartesian) filling of k-space method, but in-plane resolution may be reduced.<sup>26</sup>

As with high-resolution 3D T2W imaging, special FSE sequences, such as VISTA and SPACE, can be used as an alternative to fast GE sequences to produce high-resolution fat-suppressed T1W imaging.<sup>27</sup> They are also resistant to susceptibility artefacts, which is of utility at the skull base; a further advantage of these sequences arises from their inherent flow suppression owing to dephasing of flowing spins, which can prevent vascular time-of-flight effects simulating lesions at the skull base.<sup>28</sup> It also enables 'black blood' imaging to be performed, which helps more accurately delineate vessels, enabling superior detection of dural venous invasion by tumours as well the identification of carotid artery dissection.<sup>29,30</sup>

In general, 3D gadolinium-enhanced isotropic sequences facilitate cancer staging and treatment where the delineation of

Figure 2. Coronal reformat of 3D fat-suppressed post-gadolinium sequence through the head and skull base in a patient with primary cutaneous T-cell lymphoma demonstrates an enhancing soft-tissue mass involving Meckel's cave (upper arrowhead) and mandibular division of the trigeminal nerve (lower arrowhead). A diagnosis of neurolymphomatosis was made on the basis of imaging findings.



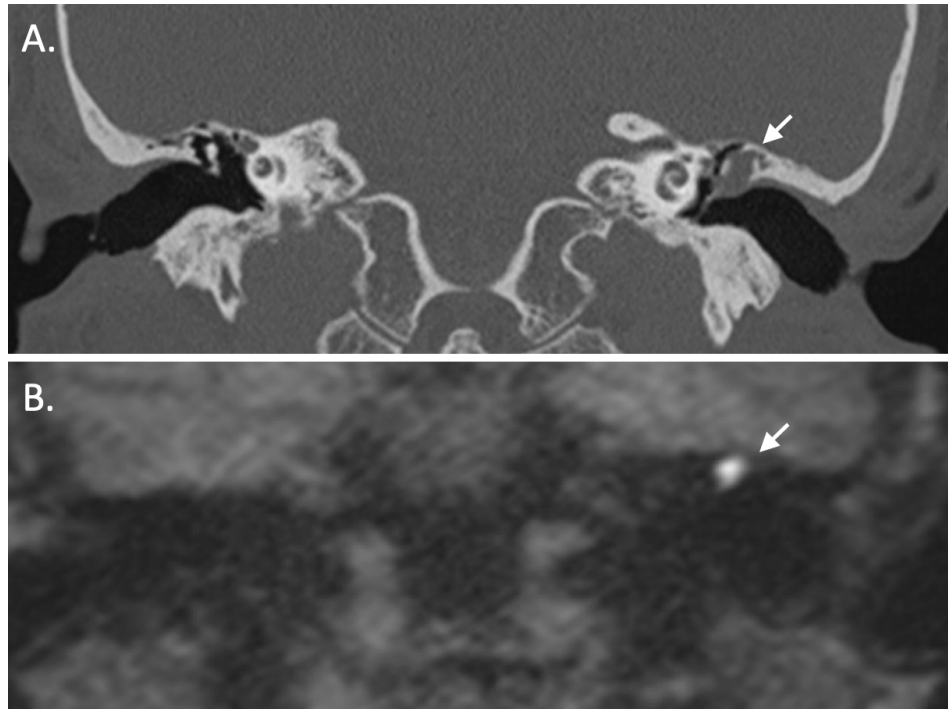
tumour extent in various planes is of paramount importance. They can also aid segmentation of important structures prior to radiotherapy<sup>31</sup> and assist in early detection of perineural spread (Figure 2).<sup>32</sup> Furthermore, they can facilitate volumetric analysis of vestibular schwannomas<sup>33</sup> as well as monitor response to stereotactic radiotherapy.<sup>34</sup>

### DIFFUSION-WEIGHTED IMAGING (DWI)

#### *DWI for middle ear and mastoid cholesteatoma*

DWI is now established as the reference imaging technique for the detection and delineation of cholesteatoma (Figure 3). It is particularly relevant in the post-operative setting where it has obviated the requirement for mandatory relook surgery in order to detect residual cholesteatoma.<sup>35</sup> TSE-based non-echo planar DWI sequences are used in order to reduce geometric distortion and susceptibility artefact, whilst allowing a high resolution matrix and thinner collimation.<sup>36</sup> Non-EPI DWI may be performed with single-shot TSE sequences such as half-Fourier or multi-shot turbo spin echo sequences such as periodically rotated overlapping parallel lines with enhanced reconstruction (PROPELLER). More recently, there has been evaluation

Figure 3. A. Coronal reformat from a CT of the temporal bones demonstrates an expansile soft tissue lesion centred on the left lateral epitympanum with scutal and ossicular erosion, compatible with a cholesteatoma (arrow). B. Coronal half-Fourier acquisition single-shot turbo spin echo (HASTE) non-EPI DWI sequence in a similar anatomical plane in the same patient demonstrates high signal within the left lateral epitympanum (arrow), which is typical of cholesteatoma. The conspicuity on such sequences is particularly helpful in the post-operative setting.



of multi-shot EPI sequences such as readout segmentation of long variable echo trains (RESOLVE) DWI, which demonstrates reduced distortion, susceptibility and T2\*blurring compared with single-shot EPI, such that the diagnostic accuracy for cholesteatoma approaches that of non-EPI methods.<sup>37</sup> The potential diagnostic value of combining the DWI sequence with other imaging data has also been demonstrated; for instance, the availability of T1W MRI sequences excludes false-positive cases (due to presumed proteinaceous or infected secretions),<sup>38</sup> whilst CT allows for better anatomical localisation,<sup>39</sup> facilitating more accurate identification of cholesteatoma. It should be noted that there remains no documented advantage in performing DWI for cholesteatoma imaging at 3T.<sup>40</sup>

Further recent studies have evaluated the role of ADC quantitation in the diagnosis of cholesteatoma. The increased DWI signal returned by keratin at  $b = 800$  or  $1000 \text{ s mm}^{-2}$  was initially felt to be predominantly due to T2 shine through; however, cholesteatoma is now known to demonstrate reduced ADC values relative to other middle ear inflammatory substrates.<sup>41,42</sup> Multiple centres have now established ADC thresholds using a range of differing techniques and scanners and have successfully differentiated cholesteatoma from non-cholesteatomatous tissue with a cut-off value of approximately  $1.3 \times 10^{-3} \text{ mm}^2 \text{ s}^{-1}$ .

Although DWI is now adopted into routine clinical practice and systematic reviews have confirmed high sensitivity (92%) and specificity (96%) of non-EPI DWI for cholesteatoma,<sup>35</sup> there has recently been more rigorous evaluation of its diagnostic accuracy

in a prospective blinded study, together with an assessment of its impact on clinical decision-making.<sup>43</sup> There remain unanswered questions as to the role of MRI in long-term surveillance of patients without clinical evidence of residual or recurrent cholesteatoma; however, long-term data are now becoming available to address this issue.<sup>44</sup>

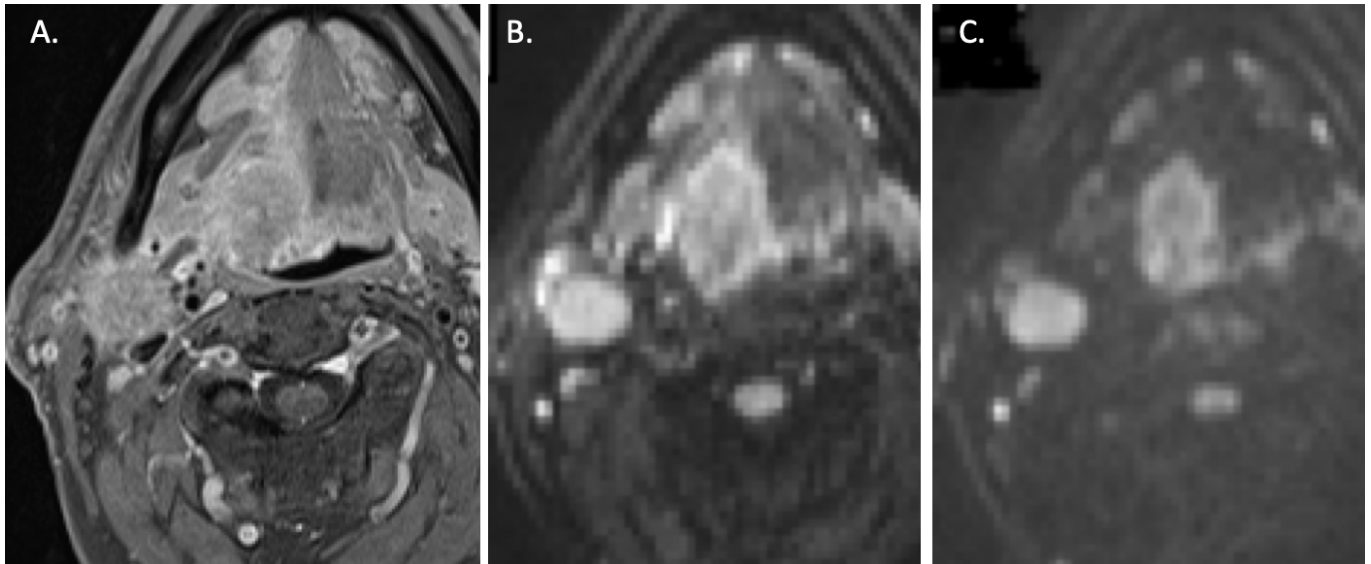
#### *DWI at other head and neck sites*

DWI has established a wider role in complementing standard MRI sequences in the characterisation of tissue and the evaluation of treatment response in the skull base, face and neck. Although the emphasis remains on head and neck carcinoma (Figure 4), recent publications have also applied DWI to diagnosis to varied tumour types at specific anatomical sites such as the pituitary gland, sinonasal region, skull base, orbit, salivary gland and thyroid gland.<sup>45-51</sup>

Most clinical and research DWI of the extracranial neck has benefitted from the high SNR and rapidity of EPI DWI; however, TSE-based DWI approaches, readout segmented EPI, integrated shimming techniques and reduced FOV imaging have been evaluated in order to reduce image distortion, which result from the multiple soft tissue air-bone interfaces and variable geometry of the head and neck.<sup>52-56</sup>

Recent research has emphasised the role of DWI in predicting the response of head and neck carcinoma to CTR either in the pre-treatment, intra-treatment or post-treatment setting. A series of studies have shown that tumours with less marked

Figure 4. Axial sequences through the neck at the level of the oropharynx. A. Axial DIXON T1w fat-suppressed post-gadolinium sequence demonstrates a right-sided tongue base tumour and an enlarged, pathological ipsilateral level 2 lymph node, but accurate delineation of the primary tumour is limited by avidly-enhancing peritumoural inflammation. B. Axial B-800 DWI sequence through the same level demonstrates increased conspicuity of the tumour. C. B-1500 DWI sequence at the same anatomical level enables clear delineation of the primary tumour with reduced signal from the peritumoural inflammatory changes.



diffusion restriction (or relatively increased ADC) on pre-treatment imaging are associated with decreased rates of locoregional control<sup>57</sup> and disease-free survival.<sup>58</sup> Intra-treatment imaging is likely to become increasingly important if response-adapted therapy, such as radiotherapy replanning with volume de-escalation and dose escalation to residual tumour, becomes the standard of care. A low percentage rise in ADC (thresholds < 14–24%) or decrease in ADC in the first few weeks after commencing CTR<sup>59</sup> has been shown to predict >2 year outcomes and hence may be used to alter the treatment strategy.<sup>60</sup> In this regard, it has been shown that DWI-based target volumes could be defined (with good interobserver agreement and with a good overlap with PET).<sup>61</sup>

In the early post-treatment phase, imaging using PET-CT is generally considered the first-line imaging to assess tumour response to CTR; however, it must be delayed until 12 weeks post-treatment due to the potential for false-positive inflammatory changes at an earlier time interval. DWI MRI also has the ability to detect residual and recurrent tumour following treatment, with a higher positive predictive value, and hence may aid in the identification of those patients who would benefit from salvage surgery. Qualitative assessment of post-treatment DWI MRI characteristically demonstrates residual tumour to be of increased DWI signal, whilst quantitative analysis applies ADC thresholds of approximately  $1.3\text{--}1.4 \times 10^{-3} \text{ mm}^2 \text{ s}^{-1}$  to distinguish it from benign post-treatment change.<sup>62</sup> MRI also has the advantage of providing a more detailed assessment of the morphological appearances and these are also of diagnostic value in distinguishing residual tumour.<sup>63</sup> The combination of DWI data and other advanced MRI techniques with that provided by PET tracers is one of the drivers behind the development of

MRI-PET hybrid systems; however, there are currently limited publications on MRI-PET outcomes in the head and neck.<sup>64,65</sup>

Different approaches to the analysis of the DWI data have also been explored in the context of predicting treatment outcomes. The propensity of head and neck carcinoma to undergo necrosis and exhibit heterogeneity may influence the mean ADC, even if attempts are made for the region of interest to exclude macroscopically visible necrosis. Hence, differing parameters such as ADC min<sup>66</sup> or methods of assessing the heterogeneity of treatment-related changes<sup>67,68</sup> may be required. Other groups have focused on the value of analysing differing b-values to help characterise tumour response. The low b-value range provides perfusion-related information and is included in the biexponential model used to define intravoxel incoherent motion parameters.<sup>69</sup> High b-values may be incorporated in calculation of mono-exponential ADC values, or may be used to perform non-Gaussian fitting, using kurtosis analysis over an extended range of b-values.<sup>70,71</sup>

However, a key issue, before these methods can be incorporated into clinical practice, is whether the repeatability of the measurements is sufficient to define any true difference in the results observed in responders versus non-responders, particularly in the post-treatment setting when regions of interest maybe more difficult to define.<sup>72</sup>

### COMPRESSED SENSING

Efforts to increase image acquisition speed have led to the development of compressed-sensing techniques that reduce the number of k-space measurements taken at acquisition.<sup>73</sup> To date, there is limited data on the applications in head and neck

imaging; however, there are imaging scenarios where the technique will likely prove to be extremely useful. This is discussed in the subsequent sections.

## PERFUSION AND PERMEABILITY IMAGING

### *Dynamic contrast-enhanced MRI*

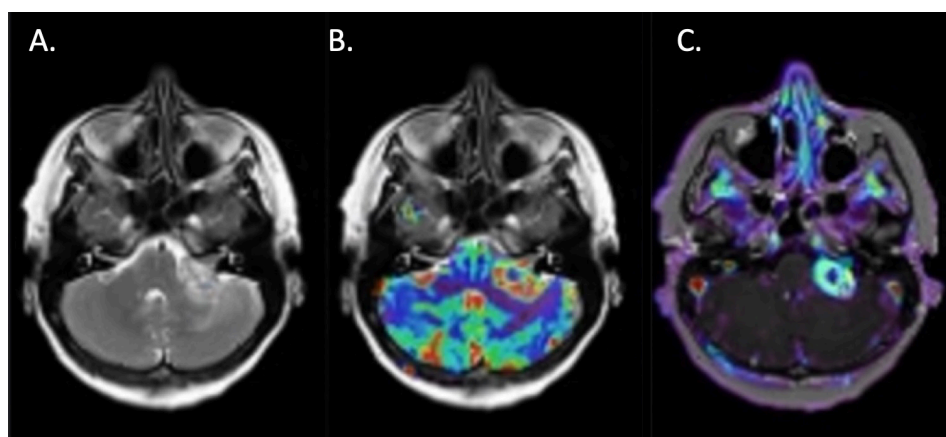
Tumour tissue is typically characterised by abnormal vascularity and permeability, which is thought influence both metastatic potential and response to therapy. The most common MRI-based approach to perfusion and permeability imaging exploits the approximately linear relationship between the signal on T1W imaging and the tissue concentration of intravenously administered gadolinium. 3D-spoiled GE sequences (*e.g.*, volumetric interpolated breath-hold examination) are commonly used to provide both pre-contrast T1 mapping (using variable flip angles to correct for B0 inhomogeneities and tissue characteristics) and post-contrast dynamic contrast imaging, resulting in a temporal resolution of  $\leq 6$  s.<sup>74</sup> Further improvements to temporal resolution can be achieved using the compressed-sensing technique golden-angle radial sparse parallel imaging.<sup>26</sup> Injection of a tight bolus of contrast ( $2\text{--}4\text{ ml s}^{-1}$  followed by a saline chaser) using a programmable power injector is essential.<sup>74,75</sup>

The simplest method of analysis of the resultant data involves the plotting of signal intensity curves, from which qualitative and semiquantitative data can be obtained. This method has been employed with some success in the evaluation of salivary gland neoplasms, with pleomorphic adenomas, Warthin tumours and salivary carcinomas demonstrating differing times to peak enhancement and washout ratios.<sup>76</sup> Latterly, Mogen *et al.*, using golden-angle radial sparse parallel imaging dynamic contrast-enhanced (DCE) MRI, found that a time-intensity curve (TIC) classification threshold of  $\geq 2$  had a high negative predictive value for malignancy and a time-intensity curve classification threshold of  $< 2$  was predictive of pleomorphic adenoma.<sup>77</sup> In head and neck SCC, a similar approach has been taken using either manually delineated ROIs or pixel-by-pixel colour-coded maps of differing TICs, with tumour tissue

typically demonstrating more rapid contrast enhancement followed by washout.<sup>78</sup> However, it is the more quantitative pharmacokinetic analysis of DCE data that has attracted the greatest attention over recent years. In particular, by employing more sophisticated mathematical modelling (*e.g.*, the extended Tofts model), various perfusion and permeability metrics can be obtained, such as the capillary permeability transfer coefficient ( $K^{\text{trans}}$ ), tumour blood volume (BV) and EEC volume ( $V_e$ ). This typically requires the placement of ROIs within tumour tissue as well as over an artery (often carotid or vertebral) in order to estimate the intravascular arterial input function.<sup>79</sup> Using this method, factors that might help to differentiate extra axial tumours, including vestibular schwannomas (Figure 5) have been explored.<sup>80</sup> Furthermore, there has been extensive work in using quantitative DCE to predict response to treatment or locoregional control have been sought, with the assumption that greater tumoural perfusion should improve response to CRT. Indeed, a recent systematic review found that a higher baseline tumour blood flow (tBF) and BV-predicted locoregional control in head and neck SCC (HNSCC).<sup>81</sup> Similarly, a higher BV 2 weeks after CRT and a persistent increase in  $K^{\text{trans}}$  were associated with locoregional control; however, after 3 weeks, this effect may reverse owing to radiation-induced inflammation.<sup>81</sup> Despite this, controversy remains with regard to the clinical utility of the technique, with select DCE-MRI parameters failing to predict long-term survival in one study of HNSCC patients.<sup>82</sup> Furthermore, interpretation of DCE-MRI results is dependent on multiple factors including intratumour and intertumour variation, hardware differences and types of algorithms employed; hence, generalisation of study outcomes can be problematic. To this end, the Quantitative Imaging Biomarkers Alliance (under the auspices of the RSNA) have sought to publish recommendations for Dual-energy CT (DECT) methodology.<sup>74</sup>

Potential alternative uses for DCE-MRI in the head and neck include the evaluation of cervical lymph nodes<sup>83</sup> and the dose-related effects of radiotherapy on mandibular bone.<sup>84</sup>

Figure 5. A. Axial T2-weighted sequence at the level of the IAM, demonstrating a left-sided vestibular schwannoma with a large extrameatal component. B. A blood volume colour map overlay has been applied demonstrating increased cerebral blood volume at the periphery of the lesion, but reduced volume within the central cystic component. C. A similar pattern is demonstrated on the  $K^{\text{trans}}$  map.



### Arterial spin labelling

As an alternative to gadolinium-based DCE, arterial spin labelling (ASL) can be performed, obviating the need for exogenous contrast injection. This typically involves the formation of a T1 map followed by magnetic labelling of blood protons before they enter the area of interest using either multiple inversion pulses (pulsed-ASL) or by invoking a pseudosteady-state (pseudocontinuous-ASL).<sup>85</sup> The latter technique offers a higher SNR and has been used in HNSCC where higher tBF prior to treatment and an increase in tBF following treatment (with small or large associated reductions in tumour volume) have been associated with subsequent local control.<sup>86</sup> More recently, ASL has been used in parotid gland tumours where tBF was significantly higher in Warthin tumours as compared to pleomorphic adenomas.<sup>87</sup> Pseudocontinuous ASL has also been employed to produce angiographic images and has been shown to provide greater diagnostic confidence over traditional time-of-flight techniques for the detection of dural arteriovenous fistulae (AVF), an important cause of pulsatile tinnitus.<sup>88</sup> This is because the ASL signal rapidly decays in the presence of normal capillary beds, but is preserved in the presence of AV shunts.<sup>88</sup>

## ADDITIONAL MRI TECHNIQUES FOR HEAD AND NECK CANCER IMAGING

### BOLD-MRI

Given that intratumoural hypoxia is associated with a reduced response to CRT, there has been interest in the blood oxygenation level-dependent (BOLD) technique, which can be used to measure the T2\* and T2 shortening effect of deoxyhaemoglobin, which is paramagnetic.<sup>59</sup> However, whilst this technique can yield quantitative oxygenation data in HNSCC, technical challenges remain, such as the effects of local, intertumoural and intratumoural variability and need to avoid measurement of necrotic tissue.<sup>89</sup> Reliability may be improved by 'oxygen-enhanced' MRI, whereby measurement is made after repeated oxygen challenges, but this method has yet to be validated in HNSCC.<sup>90</sup>

### Spectroscopy

Despite the relatively long history of MR spectroscopy (MRS), there is limited evidence for its use in the head and neck owing to a number of technical challenges.<sup>59</sup> However, 1-h MRS-derived choline/creatine ratios have utilised in combination with ADC values to successfully extract prognostic information in a cohort of patients with head and neck squamous cell carcinoma.<sup>91</sup>

### Amide proton transfer MRI

Amide proton transfer, a form of chemical exchange saturation transfer, relies upon selective saturation of amide protons using a RF pulse and subsequent exchange for water protons; this enables the minute variations in amide proton concentration associated with tumour proteins to be detected.<sup>92</sup> One study found an elevation in amide proton transfer parameters in malignant head and neck tumours when compared with normal tissues or benign salivary neoplasms, but differentiation between malignant tumour types was not possible.<sup>92</sup> The same group also found that the diagnostic improvement could be improved when combined with DWI.<sup>92</sup>

Figure 6. Venous phase of a time-resolved MRA demonstrates diffuse persistent enhancement within a left-sided jugular paraganglioma (asterisks).



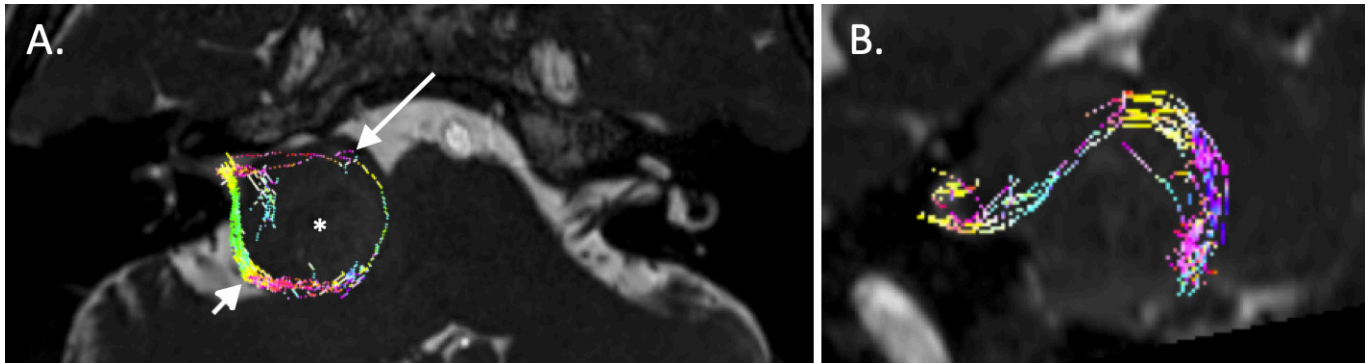
### MR elastography

Ultrasound-mediated elastography is well known, particularly with respect to thyroid imaging. However, shear-wave elastography can also be performed using MRI with an appropriate driver. With further refinement, this technique could prove useful for evaluating the differential tissue stiffness of head and neck tissues and lesions in future, circumventing limitations of ultrasound such as operator dependence and signal attenuation at depth.<sup>93</sup>

## TIME-RESOLVED MR-ANGIOGRAPHY

Time-resolved MR angiography is capable of generating images akin to digital subtraction angiography or CT-angiography (CTA), but without the disadvantage of ionising radiation. It is particularly useful in the evaluation of patients with pulsatile tinnitus or the detection of vascular tumours, such as paragangliomas (Figure 6). This technique typically involves subtracting a previously acquired mask image from a rapidly acquired dataset sampled after contrast administration, mainly from the centre of k-space, where high-contrast data is located. Various proprietary methods are in common use (e.g., time-resolved imaging of contrast kinetics (TRICKS) from GE and time-resolved angiography with interleaved stochastic trajectories (TWIST) from Siemens).<sup>6</sup> In a 2016 meta-analysis, time-resolved MR angiography demonstrated an excellent pooled sensitivity and specificity of 90 and 94%, respectively, for dural AVF, with some advantages over CTA.<sup>94</sup> The challenge of the intrinsic trade-off between temporal and spatial resolution is being addressed by acceleration methods using parallel imaging and segmented k-space ordering techniques and, more recently, radial undersampling

Figure 7. Tractography of the seventh and eighth cranial nerves using constrained spherical deconvolution. A. The tractography data have been fused with a 3D CISS sequence and demonstrates posterior displacement of a bundle of tracts thought to represent the eighth nerve (short arrow) and anterior displacement of what is thought to represent the seventh nerve (long arrow) around a large vestibular schwannoma (asterisk). B. Sagittal reconstruction from the same dataset demonstrates the extent of displacement of the posterior neural bundle.



and highly constrained reconstruction (HYPRFlow).<sup>95</sup> Such advances enable superior dural AVF characterisation.<sup>95</sup> Alternatively, compressed-sensing techniques (*e.g.*, CS-TWIST) can be employed, enabling the reduction of spatial and temporal artefacts.<sup>96</sup>

#### DIFFUSION TENSOR IMAGING

Diffusion tensor imaging (DTI) harnesses the anisotropic (directional as opposed to free) movement of water molecules in ordered human tissues (particularly neural) to perform both fibre tracking (tractography) and quantitative analysis of fractional anisotropy (FA) and mean diffusivity.

Fibre tracking algorithms enable both white matter tracts and cranial nerves to be depicted, usually with the assistance of manual placement of ROIs (or seed regions). Over the last two decades, several small studies have evaluated the use of tractography for pre-operative identification of the facial nerve in the setting of larger (>2.5 cm) vestibular schwannomas (Figure 7). In a recent systematic review, the pooled accuracy of the technique was 90.6%.<sup>97</sup> However, owing to the small study samples

and heterogeneity of algorithms and scanning parameters used, the reliability for routine use remains uncertain. Indeed, tractography techniques have evolved over recent years from deterministic single DTI (SDT), which assumes the presence of a single coherent fibre bundle, to more complex techniques that account for multiple fibre orientations within a single voxel. Such techniques include high angular resolution diffusion imaging and constrained spherical deconvolution (CSD), with the latter providing a probabilistic estimate of fibre orientation distribution. CSD in particular has shown superiority over SDT in depicting white matter fibre tracts in the brain as well as the courses of cranial nerves.<sup>98</sup> However, CSD may result in the generation of higher numbers of spurious tracts when compared with the simpler two-tensor reconstruction technique, EXtended Streamline Tractography, suggesting that resolution of complex crossing fibre patterns may be less critical for cranial nerve depiction.<sup>99</sup> In addition to depiction of the cisternal and canalicular portions of the facial nerve, tractography may aid delineation of the extracranial facial nerve prior to parotid surgery.<sup>100</sup> Furthermore, quantitative applications of DTI show promise in various settings. For instance, in one study, FA values along the auditory

Figure 8. 3D FLAIR study through the skull base at the level of the labyrinths 4 h following an injection of intravenous gadolinium. On the right, there is expansion of the cochlear duct with low-signal effacement of the scala vestibuli, compatible with cochlear hydrops (solid arrowhead); this can be compared with the normal enhancement within the left cochlea (diamond arrow). There is also effacement of the enhancing perilymphatic spaces around the right saccule and utricle, which appear enlarged and merged (open arrowhead); this can be compared with the normal left-sided vestibular enhancement (small arrow).

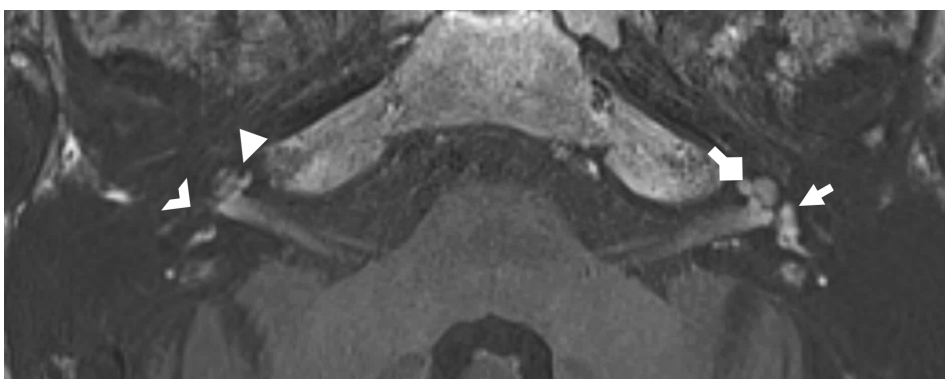
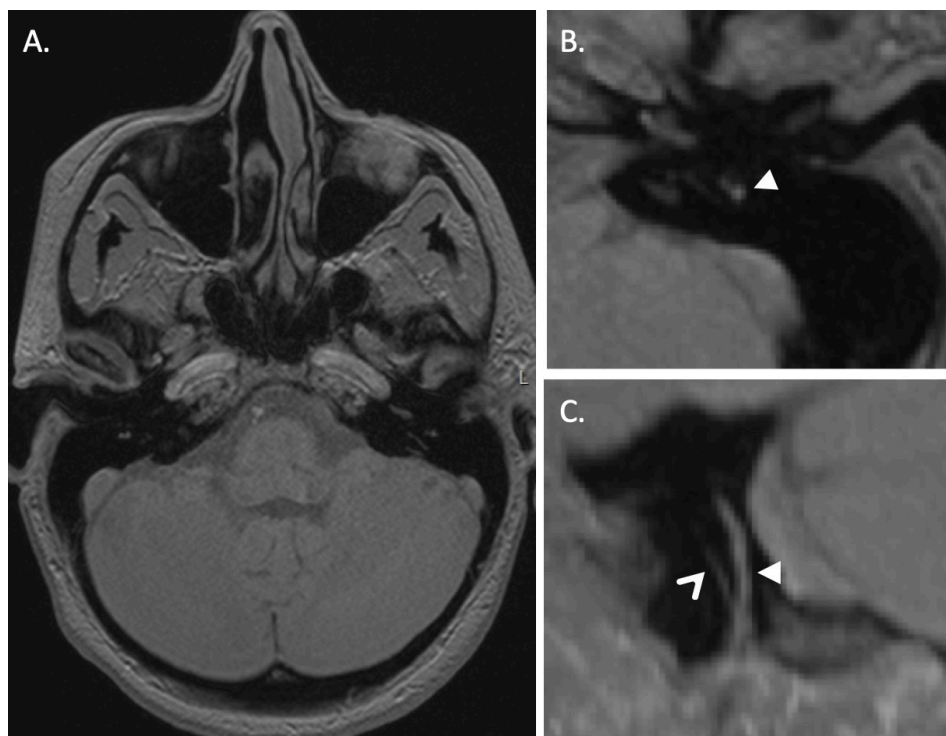


Figure 9. 3D black bone sequence through the skull base enables delineation of the intratemporal facial nerve and chorda tympani to aid posterior tympanotomy pre-operative planning. A. Axial image demonstrating the black bone acquisition which minimises soft tissue contrast, so enhancing bone-soft tissue boundaries. B. Magnified image of the left temporal bone illustrating the intermediate signal intensity nerve (solid arrowhead) surrounded by low signal within the temporal bone (and just lateral to the stapedius belly). C. Oblique sagittal image from the same sequence demonstrating the mastoid portion of the facial nerve (solid arrowhead) and chorda tympani (open arrowhead).



pathways of patients with unilateral sensorineural hearing loss were found to be lower than in controls; furthermore, there was an inverse relationship between FA and the severity of hearing impairment.<sup>101</sup> Similarly, in the setting of trigeminal neuralgia, symptomatic patients have been shown to demonstrate elevated trigeminal FA values, regardless as to whether neurovascular compression could be demonstrated on structural imaging, and higher FA values have been shown to correlate with symptom duration.<sup>102,103</sup> Such quantitative evaluation shows promise with respect to the detection and grading of severity of neural dysfunction.

### 3D FLAIR IMAGING IN OTOLOGICAL CONDITIONS

#### Endolymphatic hydrops imaging

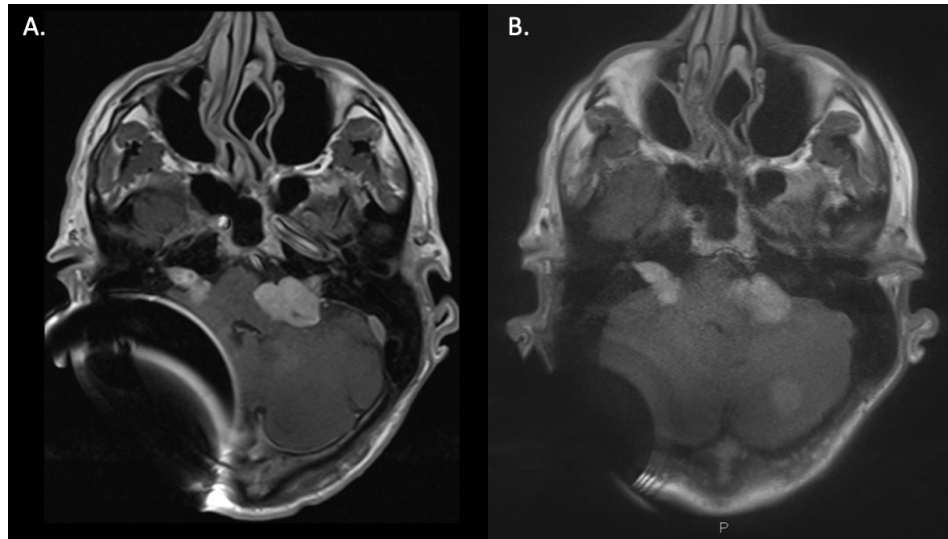
There has been considerable interest in the *in vivo* imaging of endolymphatic hydrops (EH) as a structural correlate for Meniere's disease. Although initially evaluated with intratympanic gadolinium, MRI assessment is now usually performed at 4h (0.1 or 0.2 ml kg<sup>-1</sup>) post-intravenous administration of gadolinium at 3T, which allows non-invasive visualisation of both ears. Gadolinium slowly accumulates in the perilymph but not in the endolymph, so it is possible to differentiate the enlarged endolymphatic structures (*e.g.*, utricle, saccule and cochlear duct) from the surrounding perilymph (Figure 8). 3D FLAIR sequences are most commonly used; however, 3D real inversion recovery sequences have also been assessed in this setting. Although there are longer scan times, the 3D real

inversion recovery technique is able to separate the endolymphatic space from the adjacent bone, whilst providing better resolution and contrast to noise. There is now over 10 years of accumulated MRI data using these techniques to image patients with MD and some other audiovestibular disorders.<sup>104</sup> Understandably, there is a paucity of imaging data in control subjects; however, it is recognised that EH does occur in asymptomatic individuals.<sup>105</sup> Most studies have reported their findings using various semi-quantitative scales which reference the size of the endolymphatic structures to the entire inner ear fluid space on axial sections; however, novel analytical methods are evolving.<sup>106</sup> There is some published data suggesting a role for non-gadolinium-enhanced MRI in assessing the coronal measurement of the saccule, however further studies will clarify the reproducibility of this assessment.<sup>107</sup> The current role of MRI in the diagnosis of MD remains uncertain, however identification of cochlear or vestibular hydrops on imaging may support the diagnosis in cases with incomplete phenotypes, facilitate early identification of MD, and diagnose asymptomatic contralateral changes, which may influence therapeutic strategies.

#### Sudden sensorineural hearing loss

3D FLAIR sequences have also provided new insights in the context of sudden sensorineural hearing loss, such that the role of imaging is extending beyond the exclusion of vestibular schwannoma and other retro-cochlear causes. Sudden sensorineural hearing loss is usually considered clinically idiopathic,

Figure 10. A. Standard axial post-gadolinium T1 TSE sequences through the skull base in a patient with a right-sided cochlear implant and neurofibromatosis Type 2 with bilateral vestibular schwannomas and multiple posterior fossa meningiomas. There is a large area of magnetic distortion within the right posterior fossa on the standard T1 TSE sequence, corresponding with the site of the receiver/stimulator. B. Demonstrates considerable artefact reduction following the application of slice encoding for metal artefact correction (SEMAC) (factor 14).



however increased 3D FLAIR signal within the inner ear has been observed in these patients (postulated to be due to haemorrhage or increased protein content), which may relate to infectious, immunologic, toxic or vascular aetiologies. A heavily T2W 3D FLAIR sequence can be used to increase the sensitivity to the inner ear changes.<sup>108</sup>

Whilst the presence of these imaging findings do not currently impact on treatment protocols, it has been observed that increased 3D FLAIR labyrinthine signal abnormality correlates with more severe hearing loss, poor hearing recovery and an increased incidence of vertigo.<sup>109</sup> A combination of increased 3D FLAIR and T1W intralabyrinthine high signal (a “vascular pattern”) has been correlated with particularly poor hearing outcomes.<sup>110</sup> Early phase post-gadolinium enhancement of the labyrinthine structures on 3D FLAIR sequences may reflect breakdown of the blood-labyrinth barrier and has also been assessed in a range of otologic conditions such as SSHNL, acute vestibular symptoms, otosclerosis and vestibular schwannomas.<sup>111</sup>

### BLACK BONE MRI

Black bone MRI is a novel MRI sequence designed as an alternative to CT for osseous imaging. It employs a high-resolution volumetric sequence with a short echo time (4.2 ms) and repetition time (8.6 ms) as well as a flip angle ( $5^{\circ}$ ) optimised to minimise soft tissue contrast, so enhancing bone-soft tissue boundaries. A series of papers have evaluated its potential contribution in the context of craniostylosis, craniofacial disorders, 3D cephalometry and paediatric skull fractures.<sup>112,113</sup> The lack of ionising radiation is particularly appealing for imaging of the skull base and facial skeleton in young patients and when repeated examinations are required, whilst it may also be a useful adjunct to MRI protocols used for pre-surgical planning when osseous information is required (e.g. cochlear implants) (Figure 9). This theme has been further extrapolated to the imaging of the intra-temporal facial nerve using ultra-short TE sequences (<1 ms), which capture signal from short TE tissue such as cortical bone

Table 2. Types of metal artefact reduction

Metal artefact reduction strategy	Basis of effect
View angle tilting (VAT)	Application of an additional compensated slice-selection gradient during readout resulting in a section that appears tilted.
WARP	Proprietary form of metal artefact reduction with multidirectional VAT.
Multiacquisition with variable-resonance image combination	SE sequence utilising frequency-selective excitations and multidirectional VAT with a 3D readout.
Slice encoding for metal artefact correction (SEMAC)	2D TSE technique applying additional z-phase encoding steps in the slice direction for each slice followed by algorithmic distortion correction.
Multiple slab acquisition with VAT (MSVAT)- SPACE	Multiple thin-slabs with oversampling.

Common strategies employed to reduce metal artefacts on MRI.<sup>116,117</sup>

and nerves whilst minimising susceptibility artefact at bone-air interfaces.<sup>114</sup>

## METAL ARTEFACT REDUCTION

Metal containing dental restorations as well as craniofacial implants can disrupt the homogeneity of the static magnetic field both directly and through RF-induced eddy currents, leading to image degradation with areas of signal void, geometric distortion, signal pileup and, depending on the sequence, loss of spectral fat suppression.<sup>115,116</sup> As a result, important pathology (such as oral malignancy or infection) may be obscured; hence, over recent years, considerable efforts have been directed towards mitigating these deleterious effects. Some of the common strategies are summarised in Table 2.

In a recent study using short-tau inversion recovery-based fat suppression, multiple slab acquisition with VAT-SPACE was shown to provide some advantages over SEMAC owing its capacity to generate high-resolution 3D imaging and more rapid acquisition times.<sup>115</sup> However, this situation may change with the advent of sparse-sampling (compressed) SENSE imaging, which has the capacity to significantly accelerate the SEMAC sequence.<sup>118</sup> Finally, metal artefact reduction techniques have significant utility in the setting of cochlear and other auditory implants, which may now be conditionally scanned with the magnet *in situ* (Figure 10). A SEMAC-VAT WARP technique has been successfully utilised to reduce artefact and improve image quality in the setting of an implantable bone-conduction device that would typically result in a large artefact.<sup>119</sup>

## REFERENCES

- Bieri O, Scheffler K. Fundamentals of balanced steady state free precession MRI. *J Magn Reson Imaging* 2013; **38**: 2–11. doi: <https://doi.org/10.1002/jmri.24163>
- Kojima S, Suzuki K, Hirata M, Shinohara H, Ueno E. Depicting the semicircular canals with inner-ear MRI: a comparison of the space and TrueFISP sequences. *J Magn Reson Imaging* 2013; **37**: 652–9. doi: <https://doi.org/10.1002/jmri.23863>
- Lane JL, Witte RJ, Bolster B, Bernstein MA, Johnson K, Morris J. State of the art: 3T imaging of the membranous labyrinth. *AJNR Am J Neuroradiol* 2008; **29**: 1436–40. doi: <https://doi.org/10.3174/ajnr.A1036>
- Reinshagen KL, Curtin HD, Quesnel AM, Juliano AF. Measurement for detection of incomplete partition type II anomalies on MR imaging. *AJNR Am J Neuroradiol* 2017; **38**: 2003–7. doi: <https://doi.org/10.3174/ajnr.A5335>
- Connor SEJ, Dudau C, Pai I, Gaganasiou M. Is CT or MRI the optimal imaging investigation for the diagnosis of large vestibular aqueduct syndrome and large endolymphatic sac anomaly? *Eur Arch Otorhinolaryngol* 2019; **276**: 693–702. doi: <https://doi.org/10.1007/s00405-019-05279-x>
- Tampfen M, Schwalje A, Lustig L, Alemi AS, Miller ME. Utility of preoperative computed tomography and magnetic resonance imaging in adult and pediatric cochlear implant candidates. *Laryngoscope* 2016; **126**: 1440–5. doi: <https://doi.org/10.1002/lary.25659>
- Taddeo S, Bui T, Kalle T, Koitschev A. Cochlea size in children measured in high-resolution MRI. In: *Laryngo-Rhino-Otologie*. In: Georg Thieme Verlag KG; 2019.
- Walton J, Gibson WPR, Sanli H, Prelog K. Predicting cochlear implant outcomes in children with auditory neuropathy. *Otol Neurotol* 2008; **29**: 302–9. doi: <https://doi.org/10.1097/MAO.0b013e318164d0f6>
- Buch K, Juliano A, Stankovic KM, Curtin HD, Cunnane MB. Noncontrast vestibular schwannoma surveillance imaging including an Mr cisternographic sequence: is there a need for postcontrast imaging? *J Neurosurg* 2018;: 1–6.
- Coelho DH, Tang Y, Suddarth B, Mamdani M. MRI surveillance of vestibular schwannomas without contrast enhancement: clinical and economic evaluation. *Laryngoscope* 2018; **128**: 202–9. doi: <https://doi.org/10.1002/lary.26589>
- Eljazzar R, Loewenstern J, Dai JB, Shrivastava RK, Iloreta AM. Detection of cerebrospinal fluid leaks: is there a radiologic standard of care? A systematic review. *World Neurosurg* 2019; **127**: 307–15. doi: <https://doi.org/10.1016/j.wneu.2019.01.299>
- Algin O, Berçin S, Akgunduz G, Turkbey B, Cetin H. Evaluation of labyrinthine fistula by Mr cisternography. *Emerg Radiol* 2012; **19**: 557–60. doi: <https://doi.org/10.1007/s10140-012-1050-3>
- Haller S, Etienne L, Kövari E, Varoquaux AD, Urbach H, Becker M. Imaging of neurovascular compression syndromes: trigeminal neuralgia, hemifacial spasm, vestibular paroxysmia, and glossopharyngeal neuralgia. *AJNR Am J Neuroradiol* 2016; **37**: 1384–92. doi: <https://doi.org/10.3174/ajnr.A4683>
- Hughes MA, Frederickson AM, Branstetter BF, Zhu X, Sekula RF. MRI of the trigeminal nerve in patients with trigeminal neuralgia secondary to vascular compression. *American Journal of Roentgenology* 2016; **206**: 595–600. doi: <https://doi.org/10.2214/AJR.14.14156>
- Hughes MA, Branstetter BF, Taylor CT, Fakhran S, Delfyett WT, Frederickson AM, et al. MRI findings in patients with a history of failed prior microvascular decompression for hemifacial spasm: how to image and where to look. *AJNR Am J Neuroradiol* 2015; **36**: 768–73. doi: <https://doi.org/10.3174/ajnr.A4174>
- Sivaranan N, Touska P, Murdin L, Connor SEJ. In press MRI Findings in Vestibular Paroxysmia - An Observational Study. *J Vestib Res* 2019;.
- Rommer PS, Wiest G, Kronnerwetter C, Zach H, Loader B, Elwischger K, et al. 7-Tesla MRI demonstrates absence of structural lesions in patients with vestibular paroxysmia. *Front Neuroanat* 2015; **9**: 81. doi: <https://doi.org/10.3389/fnana.2015.00081>
- van der Jagt MA, Brink WM, Versluis MJ, Steens SCA, Briare JJ, Webb AG, et al. Visualization of human inner ear anatomy with high-resolution MR imaging at 7T: initial clinical assessment. *AJNR Am J Neuroradiol* 2015; **36**: 378–83. doi: <https://doi.org/10.3174/ajnr.A4084>
- van Egmond SL, Visser F, Pameijer FA, Grolman W. In vivo imaging of the inner ear at 7T MRI. *Otology & Neurotology* 2015; **36**: 687–93. doi: <https://doi.org/10.1097/MAO.0000000000000621>
- Seitz J, Held P, Strotzer M, Völk M, Nitz WR, Dorenbeck U, et al. MR imaging of cranial nerve lesions using six different high-resolution T1- and T2(\*)-weighted 3D and 2D sequences. 2016;.
- Wendl CM, Müller S, Eiglsperger J, Fellner C, Jung EM, Meier JK. Diffusion-Weighted imaging in oral squamous cell carcinoma

- using 3 tesla MRI: is there a chance for preoperative discrimination between benign and malignant lymph nodes in daily clinical routine? *Acta Radiol* 2016; **57**: 939–46. doi: <https://doi.org/10.1177/0284185115609365>
22. Gaddikeri S, Mossa-Basha M, Andre JB, Hippe DS, Anzai Y. Optimal fat suppression in head and neck MRI: comparison of multipoint Dixon with 2 different Fat-Suppression techniques, spectral presaturation and inversion recovery, and stir. *AJNR Am J Neuroradiol* 2018; **39**: 362–8. doi: <https://doi.org/10.3174/ajnr.A5483>
  23. Qin Y, Zhang J, Li P, Wang Y. 3D double-echo steady-state with water excitation MR imaging of the intraparotid facial nerve at 1.5T: a pilot study. *AJNR Am J Neuroradiol* 2011; **32**: 1167–72. doi: <https://doi.org/10.3174/ajnr.A2480>
  24. Barkhof F, Pouwels PJW, Wattjes MP. The Holy Grail in diagnostic neuroradiology: 3T or 3D? *Eur Radiol* 2011; **21**: 449–56. doi: <https://doi.org/10.1007/s00330-010-2034-x>
  25. Ahn SS, Kim J, An C, Choi HS, Lee S-K, Koh YW, et al. Preoperative imaging evaluation of head and neck cancer: comparison of 2D spin-echo and 3D thrive MRI techniques with resected tumours. *Clin Radiol* 2012; **67**: e98–104. doi: <https://doi.org/10.1016/j.crad.2012.08.017>
  26. Wu X, Raz E, Block TK, Geppert C, Hagiwara M, Bruno MT, et al. Contrast-Enhanced radial 3D Fat-Suppressed T1-weighted gradient-recalled echo sequence versus conventional Fat-Suppressed contrast-enhanced T1-weighted studies of the head and neck. *American Journal of Roentgenology* 2014; **203**: 883–9. doi: <https://doi.org/10.2214/AJR.13.11729>
  27. Mugler JP. Optimized three-dimensional fast-spin-echo MRI. *J Magn Reson Imaging* 2014; **39**: 745–67. doi: <https://doi.org/10.1002/jmri.24542>
  28. Kato Y, Higano S, Tamura H, Mugikura S, Umetsu A, Murata T, et al. Usefulness of contrast-enhanced T1-weighted sampling perfection with application-optimized contrasts by using different FLIP angle evolutions in detection of small brain metastasis at 3T MR imaging: comparison with magnetization-prepared rapid acquisition of gradient echo imaging. *AJNR Am J Neuroradiol* 2009; **30**: 923–9. doi: <https://doi.org/10.3174/ajnr.A1506>
  29. Wang D, Lu Y, Yin B, Chen M, Geng D, Liu L, et al. 3D Fast Spin-Echo T1 Black-Blood Imaging for the Preoperative Detection of Venous Sinus Invasion by Meningioma. *Clin Neuroradiol* 2019; **29**: 65–73. doi: <https://doi.org/10.1007/s00062-017-0637-1>
  30. Edjlali M, Roca P, Rabrait C, Naggara O, Oppenheim C. 3D fast spin-echo T1 black-blood imaging for the diagnosis of cervical artery dissection. *AJNR Am J Neuroradiol* 2013; **34**: E103–E106. doi: <https://doi.org/10.3174/ajnr.A3261>
  31. Scoccianti S, Detti B, Gadda D, Greto D, Furfaro I, Meacci F, et al. Organs at risk in the brain and their dose-constraints in adults and in children: A radiation oncologist's guide for delineation in everyday practice. *Radiotherapy and Oncology* 2015; **114**: 230–8. doi: <https://doi.org/10.1016/j.radonc.2015.01.016>
  32. Freling N, Crippa F, Maroldi R. Staging and follow-up of high-grade malignant salivary gland tumours: The role of traditional versus functional imaging approaches - A review. *Oral Oncol* 2016; **60**: 157–66. doi: <https://doi.org/10.1016/j.oraloncology.2016.04.016>
  33. MacKeith S, Das T, Graves M, Patterson A, Donnelly N, Mannion R, et al. A comparison of semi-automated volumetric vs linear measurement of small vestibular schwannomas. *Eur Arch Otorhinolaryngol* 2018; **275**: 867–74. doi: <https://doi.org/10.1007/s00405-018-4865-z>
  34. Schneider T, Chapiro J, Lin M, Geschwind JF, Kleinberg L, Rigamonti D, et al. 3D quantitative assessment of response to fractionated stereotactic radiotherapy and single-session stereotactic radiosurgery of vestibular schwannoma. *Eur Radiol* 2016; **26**: 849–57. doi: <https://doi.org/10.1007/s00330-015-3895-9>
  35. Jindal M, Riskalla A, Jiang D, Connor S, O'Connor AF. A systematic review of diffusion-weighted magnetic resonance imaging in the assessment of postoperative cholesteatoma. *Otol Neurotol* 2011; **32**: 1243–9. doi: <https://doi.org/10.1097/MAO.0b013e31822e938d>
  36. Más-Estellés F, Mateos-Fernández M, Carrascosa-Bisquert B, Facal de Castro F, Puchades-Román I, Morera-Pérez C. Contemporary non-echo-planar diffusion-weighted imaging of middle ear cholesteatomas. *Radiographics* 2012; **32**: 1197–213. doi: <https://doi.org/10.1148/rg.324115109>
  37. Dudau C, Draper A, Gkagkanasiou M, Charles-Edwards G, Pai I, Connor S. Cholesteatoma: multishot echo-planar vs non echo-planar diffusion-weighted MRI for the prediction of middle ear and mastoid cholesteatoma. *BJR|Open* 2019; **1**: 20180015. doi: <https://doi.org/10.1259/bjro.20180015>
  38. Fukuda A, Morita S, Harada T, Fujiwara K, Hoshino K, Nakamaru Y, et al. Value of T1-weighted magnetic resonance imaging in cholesteatoma detection. *Otol Neurotol* 2017; **38**: 1440–4. doi: <https://doi.org/10.1097/MAO.0000000000001558>
  39. Lockett GD, Li PMMC, Fischbein NJ, Holdsworth SJ, Blevins NH. Fusion of computed tomography and propeller diffusion-weighted magnetic resonance imaging for the detection and localization of middle ear cholesteatoma. *JAMA Otolaryngol Head Neck Surg* 2016; **142**: 947. doi: <https://doi.org/10.1001/jamaoto.2016.1663>
  40. Lincot J, Veillon F, Riehm S, Babay N, Matern J-F, Rock B, et al. Middle ear cholesteatoma: compared diagnostic performances of two incremental MRI protocols including non-echo planar diffusion-weighted imaging acquired on 3T and 1.5T scanners. *J Neuroradiol* 2015; **42**: 193–201. doi: <https://doi.org/10.1016/j.neurad.2014.02.003>
  41. Cavaliere M, Di Lullo AM, Cantone E, Scala G, Elefante A, Russo C, et al. Cholesteatoma vs granulation tissue: a differential diagnosis by DWI-MRI apparent diffusion coefficient. *Eur Arch Otorhinolaryngol* 2018; **275**: 2237–43. doi: <https://doi.org/10.1007/s00405-018-5082-5>
  42. Lingam RK, Khatri P, Hughes J, Singh A. Apparent diffusion coefficients for detection of postoperative middle ear cholesteatoma on non-echo-planar diffusion-weighted images. *Radiology* 2013; **269**: 504–10. doi: <https://doi.org/10.1148/radiol.13130065>
  43. Paddle P, Hurtado G, Goergen S, Hong S, Baxter M, Copson B. Turbo spin non echo-planar diffusion weighted MRI for cholesteatoma in revision mastoidectomy: a prospective study of diagnostic accuracy and clinical impact. *Aust J Otolaryngol* 2018; **1**: 12. doi: <https://doi.org/10.21037/ajo.2018.02.02>
  44. Pai I, Crossley E, Lancer H, Dudau C, Connor S. Growth and late detection of post-operative cholesteatoma on long term follow-up with diffusion weighted magnetic resonance imaging (DWI) MRI. *Otolaryngol & Neurotology* 2019; **40**: 638–44. doi: <https://doi.org/10.1097/MAO.0000000000002188>
  45. Chen L, Xu J, Bao J, Huang X, Hu X, Xia Y, et al. Diffusion-Weighted MRI in differentiating malignant from benign thyroid nodules: a meta-analysis. *BMJ Open* 2016; **6**: e008413. doi: <https://doi.org/10.1136/bmjopen-2015-008413>
  46. Sepahdari AR, Politi LS, Aakalu VK, Kim HJ, Razek AAKA. Diffusion-Weighted imaging of orbital masses: multi-institutional data support a 2-ADC threshold model to categorize lesions as benign, malignant, or indeterminate. *AJNR*

- Am J Neuroradiol* 2014; **35**: 170–5. doi: <https://doi.org/10.3174/ajnr.A3619>
47. Wang M, Liu H, Wei X, Liu C, Liang T, Zhang X, et al. Application of Reduced-FOV diffusion-weighted imaging in evaluation of normal pituitary glands and pituitary macroadenomas. *AJNR Am J Neuroradiol* 2018; **39**: 1499–504.
  48. Wang F, Sha Y, Zhao M, Wan H, Zhang F, Cheng Y, et al. High-Resolution diffusion-weighted imaging improves the diagnostic accuracy of dynamic contrast-enhanced sinonasal magnetic resonance imaging. *J Comput Assist Tomogr* 2017; **41**: 199–205. doi: <https://doi.org/10.1097/RCT.0000000000000502>
  49. Abdel Razek A, Mossad A, Ghonim M. Role of diffusion-weighted MR imaging in assessing malignant versus benign skull-base lesions. *Radiol Med* 2011; **116**: 125–32. doi: <https://doi.org/10.1007/s11547-010-0588-y>
  50. Yuan Y, Tang W, Tao X. Parotid gland lesions: separate and combined diagnostic value of conventional MRI, diffusion-weighted imaging and dynamic contrast-enhanced MRI. *Br J Radiol* 2016; **89**: 20150912. doi: <https://doi.org/10.1259/bjr.20150912>
  51. Yuan Y, Shi H, Tao X. Head and neck paragangliomas: diffusion weighted and dynamic contrast enhanced magnetic resonance imaging characteristics. *BMC Med Imaging* 2016; **16**: 12. doi: <https://doi.org/10.1186/s12880-016-0114-3>
  52. Juan C-J, Chang H-C, Hsueh C-J, Liu H-S, Huang Y-C, Chung H-W, et al. Salivary glands: echo-planar versus propeller diffusion-weighted MR imaging for assessment of ADCs. *Radiology* 2009; **253**: 144–52. doi: <https://doi.org/10.1148/radiol.2531082228>
  53. Schakel T, Hoogduin JM, Terhaard CHJ, Philippens MEP. Technical note: diffusion-weighted MRI with minimal distortion in head-and-neck radiotherapy using a turbo spin echo acquisition method. *Med Phys* 2017; **44**: 4188–93. doi: <https://doi.org/10.1002/mp.12363>
  54. Taviani V, Nagala S, Priest AN, McLean MA, Jani P, Graves MJ. 3T diffusion-weighted MRI of the thyroid gland with reduced distortion: preliminary results. *Br J Radiol* 2013; **86**: 20130022. doi: <https://doi.org/10.1259/bjr.20130022>
  55. Verhappen MH, Pouwels PJW, Ljumanovic R, van der Putten L, Knol DL, De Bree R, et al. Diffusion-Weighted MR imaging in head and neck cancer: comparison between half-fourier acquired single-shot turbo spin-echo and epi techniques. *AJNR Am J Neuroradiol* 2012; **33**: 1239–46. doi: <https://doi.org/10.3174/ajnr.A2949>
  56. Gatidis S, Graf H, Weiß J, Stemmer A, Kiefer B, Nikolaou K, et al. Diffusion-weighted echo planar MR imaging of the neck at 3 T using integrated shimming: comparison of MR sequence techniques for reducing artifacts caused by magnetic-field inhomogeneities. *MAGMA* 2017; **30**: 57–63. doi: <https://doi.org/10.1007/s10334-016-0582-z>
  57. Lambrecht M, Van Calster B, Vandecaveye V, De Keyzer F, Roebben I, Hermans R, et al. Integrating pretreatment diffusion weighted MRI into a multivariable prognostic model for head and neck squamous cell carcinoma. *Radiother Oncol* 2014; **110**: 429–34. doi: <https://doi.org/10.1016/j.radonc.2014.01.004>
  58. Noij DP, Pouwels PJW, Ljumanovic R, Knol DL, Doornaert P, de Bree R, et al. Predictive value of diffusion-weighted imaging without and with including contrast-enhanced magnetic resonance imaging in image analysis of head and neck squamous cell carcinoma. *Eur J Radiol* 2015; **84**: 108–16. doi: <https://doi.org/10.1016/j.ejrad.2014.10.015>
  59. King AD, Thoeny HC. Functional MRI for the prediction of treatment response in head and neck squamous cell carcinoma: potential and limitations. *Cancer Imaging* 2016; **16**: 23. doi: <https://doi.org/10.1186/s40644-016-0080-6>
  60. Matoba M, Tuji H, Shimode Y, Toyoda I, Kuginuki Y, Miwa K, et al. Fractional change in apparent diffusion coefficient as an imaging biomarker for predicting treatment response in head and neck cancer treated with chemoradiotherapy. *AJNR Am J Neuroradiol* 2014; **35**: 379–85. doi: <https://doi.org/10.3174/ajnr.A3706>
  61. Schakel T, Peltenburg B, Dankbaar J-W, Cardenas CE, Aristophanous M, Terhaard CHJ, et al. Evaluation of diffusion weighted imaging for tumor delineation in head-and-neck radiotherapy by comparison with automatically segmented 18 F-fluorodeoxyglucose positron emission tomography. *Phys Imaging Radiat Oncol* 2018; **5**: 13–18. doi: <https://doi.org/10.1016/j.phro.2017.12.004>
  62. King AD, Mo FKF, Yu K-H, Yeung DKW, Zhou H, Bhatia KS, et al. Squamous cell carcinoma of the head and neck: diffusion-weighted MR imaging for prediction and monitoring of treatment response. *Eur Radiol* 2010; **20**: 2213–20. doi: <https://doi.org/10.1007/s00330-010-1769-8>
  63. Ailianou A, Mundada P, De Perrot T, Pusztašzieri M, Poletti P-A, Becker M. Mri with DWI for the detection of posttreatment head and neck squamous cell carcinoma: why morphologic MRI criteria matter. *AJNR Am J Neuroradiol* 2018; **39**: 748–55. doi: <https://doi.org/10.3174/ajnr.A5548>
  64. Covello M, Cavaliere C, Aiello M, Cianelli MS, Mesolella M, Iorio B, et al. Simultaneous PET/MR head-neck cancer imaging: preliminary clinical experience and multiparametric evaluation. *Eur J Radiol* 2015; **84**: 1269–76. doi: <https://doi.org/10.1016/j.ejrad.2015.04.010>
  65. Rasmussen JH, Nørgaard M, Hansen AE, Vogelius IR, Aznar MC, Johannesen HH, et al. Feasibility of multiparametric imaging with PET/MR in head and neck squamous cell carcinoma. *J Nucl Med* 2017; **58**: 69–74. doi: <https://doi.org/10.2967/jnumed.116.180091>
  66. Preda L, Conte G, Bonello L, Giannitto C, Travaini LL, Raimondi S, et al. Combining standardized uptake value of FDG-PET and apparent diffusion coefficient of DW-MRI improves risk stratification in head and neck squamous cell carcinoma. *Eur Radiol* 2016; **26**: 4432–41. doi: <https://doi.org/10.1007/s00330-016-4284-8>
  67. Galbán CJ, Mukherji SK, Chenevert TL, Meyer CR, Hamstra DA, Bland PH, et al. A feasibility study of parametric response MAP analysis of diffusion-weighted magnetic resonance imaging scans of head and neck cancer patients for providing early detection of therapeutic efficacy. *Transl Oncol* 2009; **2**: 184–90. doi: <https://doi.org/10.1593/tlo.09175>
  68. King AD, Chow K-K, Yu K-H, Mo FKF, Yeung DKW, Yuan J, et al. Head and neck squamous cell carcinoma: diagnostic performance of diffusion-weighted MR imaging for the prediction of treatment response. *Radiology* 2013; **266**: 531–8. doi: <https://doi.org/10.1148/radiol.12120167>
  69. Xiao-ping Y, Jing H, Fei-ping L, Yin H, Qiang L, Lanlan W, et al. Intravoxel incoherent motion MRI for predicting early response to induction chemotherapy and chemoradiotherapy in patients with nasopharyngeal carcinoma. *J Magn Reson Imaging* 2016; **43**: 1179–90. doi: <https://doi.org/10.1002/jmri.25075>
  70. Ryoo I, Kim J-H, Choi SH, Sohn C-H, Kim SC. Squamous Cell Carcinoma of the Head and Neck: Comparison of Diffusion-weighted MRI at b-values of 1,000 and 2,000 s/mm<sup>2</sup> to Predict Response to Induction Chemotherapy. *Magn Reson Med Sci* 2015; **14**: 337–45. doi: <https://doi.org/10.2463/mrms.2015-0003>
  71. Fujima N, Sakashita T, Homma A, Yoshida D, Kudo K, Shirato H. Utility of a hybrid IVIM-DKI model to predict the

- development of distant metastasis in head and neck squamous cell carcinoma patients. *Magn Reson Med Sci* 2018; **17**: 21–7. doi: <https://doi.org/10.2463/mrms.mp.2016-0136>
72. Hoang JK, Choudhury KR, Chang J, Craciunescu OI, Yoo DS, Brizel DM. Diffusion-Weighted imaging for head and neck squamous cell carcinoma: quantifying repeatability to understand early treatment-induced change. *AJR Am J Roentgenol* 2014; **203**: 1104–8. doi: <https://doi.org/10.2214/AJR.14.12838>
  73. Jaspan ON, Fleysher R, Lipton ML. Compressed sensing MRI: a review of the clinical literature. *Br J Radiol* 2015; **88**: 20150487. doi: <https://doi.org/10.1259/bjr.20150487>
  74. Shukla-Dave A, Obuchowski NA, Chenevert TL, Jambawalikar S, Schwartz LH, Malyarenko D, et al. Quantitative imaging biomarkers alliance (QIBA) recommendations for improved precision of DWI and DCE-MRI derived biomarkers in multicenter oncology trials. *J Magn Reson Imaging* 2019; **49**: e101–e121. doi: <https://doi.org/10.1002/jmri.26518>
  75. Jansen JFA, Parra C, Lu Y, Shukla-Dave A. Evaluation of head and neck tumors with functional MR imaging. *Magn Reson Imaging Clin N Am* 2016; **24**: 123–33. doi: <https://doi.org/10.1016/j.mric.2015.08.011>
  76. Lam PD, Kuribayashi A, Imaizumi A, Sakamoto J, Sumi Y, Yoshino N, et al. Differentiating benign and malignant salivary gland tumours: diagnostic criteria and the accuracy of dynamic contrast-enhanced MRI with high temporal resolution. *Br J Radiol* 2015; **88**: 20140685. doi: <https://doi.org/10.1259/bjr.20140685>
  77. Mogen JL, Block KT, Bansal NK, Patrie JT, Mukherjee S, Zan E, et al. Dynamic contrast-enhanced MRI to differentiate parotid neoplasms using Golden-Angle radial sparse parallel imaging. *AJNR Am J Neuroradiol* 2019; **40**: 1029–36. doi: <https://doi.org/10.3174/ajnr.A6055>
  78. Yuan J, Chow SKK, Yeung DKW, King AD. A five-colour colour-coded mapping method for DCE-MRI analysis of head and neck tumours. *Clin Radiol* 2012; **67**: 216–23. doi: <https://doi.org/10.1016/j.crad.2011.07.052>
  79. Chikui T, Obara M, Simonetti AW, Ohga M, Koga S, Kawano S, et al. The principal of dynamic contrast enhanced MRI, the method of pharmacokinetic analysis, and its application in the head and neck region. *Int J Dent* 2012; **2012**: 1–10. doi: <https://doi.org/10.1155/2012/480659>
  80. Zimny A, Sasiadek M. Contribution of perfusion-weighted magnetic resonance imaging in the differentiation of meningiomas and other extra-axial tumors: case reports and literature review. *J Neurooncol* 2011; **103**: 777–83. doi: <https://doi.org/10.1007/s11060-010-0445-9>
  81. Martens RM, Noij DP, Ali M, Koopman T, Marcus JT, Vergeer MR, et al. Functional imaging early during (chemo)radiotherapy for response prediction in head and neck squamous cell carcinoma; a systematic review. *Oral Oncol* 2019; **88**: 75–83. doi: <https://doi.org/10.1016/j.oraloncology.2018.11.005>
  82. Lowe NM, Kershaw LE, Bernstein JM, Withey SB, Mais K, Homer JJ, et al. Pre-Treatment tumour perfusion parameters and initial RECIST response do not predict long-term survival outcomes for patients with head and neck squamous cell carcinoma treated with induction chemotherapy. *PLoS One* 2018; **13**: e0194841. doi: <https://doi.org/10.1371/journal.pone.0194841>
  83. Shukla-Dave A, Lee NY, Jansen JFA, Thaler HT, Stambuk HE, Fury MG, et al. Dynamic contrast-enhanced magnetic resonance imaging as a predictor of outcome in head-and-neck squamous cell carcinoma patients with nodal metastases. *Int J Radiat Oncol Biol Phys* 2012; **82**: 1837–44. doi: <https://doi.org/10.1016/j.ijrobp.2011.03.006>
  84. Sandulache VC, Hobbs BP, Mohamed ASR, Frank SJ, Song J, Ding Y, et al. Dynamic contrast-enhanced MRI detects acute radiotherapy-induced alterations in mandibular microvasculature: prospective assessment of imaging biomarkers of normal tissue injury. *Sci Rep* 2016; **6**: 29864.
  85. Haller S, Zaharchuk G, Thomas DL, Lovblad K-O, Barkhof F, Golay X. Arterial spin labeling perfusion of the brain: emerging clinical applications. *Radiology* 2016; **281**: 337–56. doi: <https://doi.org/10.1148/radiol.2016150789>
  86. Fujima N, Yoshida D, Sakashita T, Homma A, Tsukahara A, Tha KK, et al. Usefulness of Pseudocontinuous arterial spin-labeling for the assessment of patients with head and neck squamous cell carcinoma by measuring tumor blood flow in the pretreatment and early treatment period. *AJNR Am J Neuroradiol* 2016; **37**: 342–8. doi: <https://doi.org/10.3174/ajnr.A4513>
  87. Yamamoto T, Kimura H, Hayashi K, Imamura Y, Mori M. Pseudo-continuous arterial spin labeling Mr images in Warthin tumors and pleomorphic adenomas of the parotid gland: qualitative and quantitative analyses and their correlation with histopathologic and DWI and dynamic contrast enhanced MRI findings. *Neuroradiology* 2018; **60**: 803–12. doi: <https://doi.org/10.1007/s00234-018-2046-9>
  88. Amukotuwa SA, Marks MP, Zaharchuk G, Calamante F, Bammer R, Fischbein N. Arterial spin-labeling improves detection of intracranial dural arteriovenous fistulas with MRI. *AJNR Am J Neuroradiol* 2018; **39**: 669–77. doi: <https://doi.org/10.3174/ajnr.A5570>
  89. Panek R, Welsh L, Dunlop A, Wong KH, Riddell AM, Koh D-M, et al. Repeatability and sensitivity of T2\* measurements in patients with head and neck squamous cell carcinoma at 3T. *J Magn Reson Imaging* 2016; **44**: 72–80. doi: <https://doi.org/10.1002/jmri.25134>
  90. Dewhirst MW, Birer SR. Oxygen-Enhanced MRI is a major advance in tumor hypoxia imaging. *Cancer Res* 2016; **76**: 769–72. doi: <https://doi.org/10.1158/0008-5472.CAN-15-2818>
  91. Razek AAKA, Nada N. Correlation of Choline/Creatine and apparent diffusion coefficient values with the prognostic parameters of head and neck squamous cell carcinoma. *NMR Biomed* 2016; **29**: 483–9. doi: <https://doi.org/10.1002/nbm.3472>
  92. Law BKH, King AD, Ai Q-Y, Poon DMC, Chen W, Bhatia KS, et al. Head and neck tumors: amide proton transfer MRI. *Radiology* 2018; **288**: 782–90. doi: <https://doi.org/10.1148/radiol.2018171528>
  93. Yeung DKW, Bhatia KS, Lee YYP, King AD, Garteiser P, Sinku R, et al. Mr elastography of the head and neck: driver design and initial results. *Magn Reson Imaging* 2013; **31**: 624–9. doi: <https://doi.org/10.1016/j.mri.2012.09.008>
  94. Lin Y-H, Lin H-H, Liu H-M, Lee C-W, Chen Y-F. Diagnostic performance of CT and MRI on the detection of symptomatic intracranial dural arteriovenous fistula: a meta-analysis with indirect comparison. *Neuroradiology* 2016; **58**: 753–63. doi: <https://doi.org/10.1007/s00234-016-1696-8>
  95. Clark Z, Johnson KM, Wu Y, Edjlali M, Mistretta C, Wieben O, et al. Accelerated time-resolved contrast-enhanced magnetic resonance angiography of dural arteriovenous fistulas using highly constrained reconstruction of sparse cerebrovascular data sets. *Invest Radiol* 2016; **51**: 365–71. doi: <https://doi.org/10.1097/RLL.0000000000000212>
  96. Rapacchi S, Natsuaki Y, Plotnik A, Gabriel S, Laub G, Finn JP, et al. Reducing view-sharing using compressed sensing in time-resolved contrast-enhanced magnetic resonance angiography. *Magn. Reson. Med.*

- 2015; **74**: 474–81. doi: <https://doi.org/10.1002/mrm.25414>
97. Savardekar AR, Patra DP, Thakur JD, Narayan V, Mohammed N, Bollam P, et al. Preoperative diffusion tensor imaging–fiber tracking for facial nerve identification in vestibular schwannoma: a systematic review on its evolution and current status with a pooled data analysis of surgical concordance rates. *Neurosurg Focus* 2018; **44**: E5. doi: <https://doi.org/10.3171/2017.12.FOCUS17672>
  98. Zolal A, Sobottka SB, Podlesek D, Linn J, Rieger B, Juratli TA, et al. Comparison of probabilistic and deterministic fiber tracking of cranial nerves. *J Neurosurg* 2017; **127**: 613–21. doi: <https://doi.org/10.3171/2016.8.JNS16363>
  99. Behan B, Chen DQ, Sammartino F, DeSouza DD, Wharton-Shukster E, Hodaie M. Comparison of diffusion-weighted MRI reconstruction methods for visualization of cranial nerves in posterior fossa surgery. *Front Neurosci* 2017; **11**: 554. doi: <https://doi.org/10.3389/fnins.2017.00554>
  100. Attyé A, Karkas A, Tropès I, Roustit M, Kastler A, Bettega G, et al. Parotid gland tumours: Mr tractography to assess contact with the facial nerve. *Eur Radiol* 2016; **26**: 2233–41. doi: <https://doi.org/10.1007/s00330-015-4049-9>
  101. Kim S, Kwon HJ, Kang E-J, Kim DW. Diffusion-Tensor tractography of the auditory neural pathway. *Clin Neuroradiol* 2018; **1**–8.
  102. Lutz J, Thon N, Stahl R, Lummel N, Tonn J-C, Linn J, et al. Microstructural alterations in trigeminal neuralgia determined by diffusion tensor imaging are independent of symptom duration, severity, and type of neurovascular conflict. *J Neurosurg* 2016; **124**: 823–30. doi: <https://doi.org/10.3171/2015.2.JNS142587>
  103. Lee C-C, Chong ST, Chen C-J, Hung S-C, Yang H-C, Lin C-J, et al. The timing of stereotactic radiosurgery for medically refractory trigeminal neuralgia: the evidence from diffusion tractography images. *Acta Neurochir* 2018; **160**: 977–86. doi: <https://doi.org/10.1007/s00701-017-3449-9>
  104. Nakashima T, Naganawa S, Sugiura M, Teranishi M, Sone M, Hayashi H, et al. Visualization of endolymphatic hydrops in patients with Meniere's disease. *Laryngoscope* 2007; **117**: 415–20. doi: <https://doi.org/10.1097/MLG.0b013e31802c300c>
  105. Baráth K, Schuknecht B, Naldi AM, Schrepfer T, Bockisch CJ, Hegemann SCA. Detection and grading of endolymphatic hydrops in Menière disease using MR imaging. *AJNR Am J Neuroradiol* 2014; **35**: 1387–92. doi: <https://doi.org/10.3174/ajnr.A3856>
  106. Attyé A, Eliezer M, Boudiaf N, Tropes I, Chechin D, Schmerber S, et al. Mri of endolymphatic hydrops in patients with Meniere's disease: a case-controlled study with a simplified classification based on saccular morphology. *Eur Radiol* 2017; **27**: 3138–46. doi: <https://doi.org/10.1007/s00330-016-4701-z>
  107. Venkatasamy A, Veillon F, Fleury A, Eliezer M, Abu Eid M, Romain B, et al. Imaging of the sacculle for the diagnosis of endolymphatic hydrops in Meniere disease, using a three-dimensional T2-weighted steady state free precession sequence: accurate, fast, and without contrast material intravenous injection. *Eur Radiol Exp* 2017; **1**: 14. doi: <https://doi.org/10.1186/s41747-017-0020-7>
  108. Naganawa S, Kawai H, Taoka T, Suzuki K, Iwano S, Satake H, et al. Heavily T<sub>2</sub>-Weighted 3D-FLAIR improves the detection of cochlear lymph fluid signal abnormalities in patients with sudden sensorineural hearing loss. *Magn Reson Med Sci* 2016; **15**: 203–11. doi: <https://doi.org/10.2463/mrms.mp.2015-0065>
  109. Gao Z, Chi F-lu. The clinical value of three-dimensional fluid-attenuated inversion recovery magnetic resonance imaging in patients with idiopathic sudden sensorineural hearing loss: a meta-analysis. *Otol Neurotol* 2014; **35**: 1730–5. doi: <https://doi.org/10.1097/MAO.0000000000000611>
  110. Lee JW, Park YA, Park SM, Kong TH, Park SY, Bong JP, et al. Clinical features and prognosis of sudden sensorineural hearing loss secondary to Intralabyrinthine hemorrhage. *J Audiol Otol* 2016; **20**: 31–5. doi: <https://doi.org/10.7874/jao.2016.20.1.31>
  111. Eliezer M, Maquet C, Horion J, Gillibert A, Toupet M, Bolognini B, et al. Detection of intralabyrinthine abnormalities using post-contrast delayed 3D-FLAIR MRI sequences in patients with acute vestibular syndrome. *Eur Radiol* 2019; **29**: 2760–9. doi: <https://doi.org/10.1007/s00330-018-5825-0>
  112. Eley KA, McIntyre AG, Watt-Smith SR, Golding SJ. "Black bone" MRI: a partial flip angle technique for radiation reduction in craniofacial imaging. *Br J Radiol* 2012; **85**: 272–8. doi: <https://doi.org/10.1259/bjr/95110289>
  113. Eley KA, Watt-Smith SR, Sheerin F, Golding SJ. "Black Bone" MRI: a potential alternative to CT with three-dimensional reconstruction of the craniofacial skeleton in the diagnosis of craniosynostosis. *Eur Radiol* 2014; **24**: 2417–26. doi: <https://doi.org/10.1007/s00330-014-3286-7>
  114. Guenette JP, Seethamraju RT, Jayender J, Corrales CE, Lee TC. Mr imaging of the facial nerve through the temporal bone at 3T with a noncontrast ultrashort echo time sequence. *AJNR Am J Neuroradiol* 2018; **39**: 1903–6. doi: <https://doi.org/10.3174/ajnr.A5754>
  115. Hilgenfeld T, Prager M, Schwindling FS, Nittka M, Rammelsberg P, Bendszus M, et al. MSVAT-SPACE-STIR and SEMAC-STIR for reduction of metallic artifacts in 3T head and neck MRI. *AJNR Am J Neuroradiol* 2018; **39**: 1322–9. doi: <https://doi.org/10.3174/ajnr.A5678>
  116. Ai T, Padua A, Goerner F, Nittka M, Gugala Z, Jadhav S, et al. SEMAC-VAT and MSVAT-SPACE sequence strategies for metal artifact reduction in 1.5T magnetic resonance imaging. *Invest Radiol* 2012; **47**: 267–76. doi: <https://doi.org/10.1097/RLI.0b013e318240a919>
  117. Talbot BS, Weinberg EP. Mr imaging with Metal-suppression sequences for evaluation of total joint arthroplasty. *Radiographics* 2016; **36**: 209–25. doi: <https://doi.org/10.1148/rg.2016150075>
  118. Otazo R, Nittka M, Bruno M, Raithe E, Geppert C, Gyftopoulos S, et al. Sparse-SEMAC: rapid and improved SEMAC metal implant imaging using SPARSE-SENSE acceleration. *Magn Reson Med* 2017; **78**: 79–87. doi: <https://doi.org/10.1002/mrm.26342>
  119. Wimmer W, Hakim A, Kiefer C, Pastore-Wapp M, Anschuetz L, Caversaccio MD, et al. Mri metal artifact reduction sequence for auditory implants: first results with a transcutaneous bone conduction implant. *Audiol Neurotol* 2019; **1**–9.